Electromechanical Energy Conversion Systems (EECS)
Niroo Research Institute (NRI)
Vol. 5, No. 1, Autumn 2026, pp. 41-52
DOI: 10.30503/eecs.2026.603929.1083
Research Article

DOE-Based Torque Profile Optimization of a Novel Magnetic Gear Considering Vibration Characteristics

Mahdi Abolghasemi[1,2*], Aghil Ghaheri[1], Mohammad Mardani[1], Seyyed Ebrahim Afjei[1]

Abstract

In this study, a novel Double-Layer Radial-Flux Magnetic Gear (DLRFMG) is developed and systematically investigated to enhance torque transmission capability while mitigating torque ripple. The proposed configuration incorporates two successive torque-conversion stages, allowing the magnetic gear to achieve an increased transmission ratio and improved torque performance. A Taguchi-based optimization procedure employing an L27 orthogonal array was implemented to determine the influence of the design parameters on the maximum transferable torque and torque ripple of the rotors while limiting the required number of numerical experiments. The optimization results indicate that the proposed design can increase the maximum torque by up to 66.71% and decrease torque ripple by more than 60% relative to the initial configuration. In addition, analysis of variance (ANOVA) was performed to quantify the contribution of the investigated parameters and determine the most influential design factors. The optimized DLRFMG consequently provides improved torque characteristics and demonstrates considerable potential for power transmission applications in electric transportation, electric bicycles, and renewable energy systems. Furthermore, static structural and modal analyses were performed to investigate the effects of the optimized torque profile on the mechanical integrity and vibration characteristics of the DLRFMG. The results show that the optimized configuration maintains acceptable structural displacements and exhibits sufficiently high natural frequencies, confirming that the enhanced electromagnetic performance is achieved without compromising the mechanical stability of the magnetic gear.

Keywords: Magnetic Gear, Optimization, Permanent Magnet, Taguchi Method, Vibration.

Received Date: 2026-09-22; Revised Date: 2026-11-21; Accepted Date: 2026-11-25 .

1. INTRODUCTION

Gear transmission systems are widely used in automotive, industrial, material-handling, electric-bicycle, and wind-energy applications. Conventional mechanical gears rely on physical tooth contact, leading to friction losses, lubrication requirements, acoustic noise, wear, and possible tooth failure [1,2]. Magnetic gears provide a contactless alternative in which torque is transferred through magnetic interactions, eliminating conventional lubrication and significantly reducing mechanical wear and noise [3,4]. Their high reliability and low maintenance requirements make them attractive for demanding applications.

The development of magnetic gearing extends back more than a century, beginning with Armstrong's electromagnetically actuated gear concept in 1901 [5] and Faus's permanent-magnet-based magnetic gear in the 1940s [6]. Early designs were limited by the low torque density of ferrite magnets, while the introduction of high-energy rare-earth PMs substantially improved their performance [7,8]. A major advance was the concentric magnetic gear introduced by Atallah and Howe in 2001, which demonstrated high torque transmission in a coaxial arrangement [9]. Subsequent harmonic analyses clarified the magnetic-field modulation mechanism and supported the selection of suitable topologies for different applications [10]. Comparative investigations reported in [11] further indicated that concentric magnetic gear configurations can provide a relatively high torque density. Various studies have investigated methods to improve magnetic-gear performance through electromagnetic and geometric modifications. Spoke-type PMs have been employed to reduce end effects and enhance transferable torque [12], while air-gap dimensions strongly influence leakage flux and torque capability [13]. Angular and transverse misalignments can degrade torque transmission [14], whereas increasing the axial stack length can mitigate end effects [15]. These studies highlight the importance of simultaneously considering electromagnetic and geometric parameters in magnetic-gear design.

Optimization techniques have also received considerable attention in the design of magnetic gears. The Taguchi method was employed in [16,17] to simultaneously optimize maximum torque and torque ripple for multiple rotors, demonstrating its capability for multi-objective parameter optimization. A similar methodology was adopted in [18] to improve the torque transmission performance of a magnetic gear. Other approaches,

[1] *Department of Electrical Engineering, Shahid Beheshti University, Tehran, Iran*
[2] *Khorasan-Razavi Electric Distribution Company (KEDC), Mashhad, Iran*
**Corresponding author, Email: m.abolghasemi@hotmail.com*
@ 2026 Niroo Research Institute, All rights reserved.

such as genetic algorithms, can provide high optimization accuracy but generally require many iterations and high computational cost [19]. In contrast, the Taguchi method, as a Design of Experiments (DOE) technique, evaluates the effects of multiple parameters using a limited number of strategically selected simulations [20]. The applicability of the Taguchi approach has also been demonstrated in related electromagnetic and electromechanical systems. In [21], Taguchi-based optimization was used to improve structural performance through cogging-torque reduction, while the resulting analysis indicated that the product performance exhibited limited sensitivity to manufacturing-related variations. A sequential Taguchi strategy was proposed in [22] for Switched Reluctance Motor (SRM) drive systems, leading to increased average torque, reduced torque ripple, and improved robustness relative to the initial design. In another investigation, modification of the rotor outer diameter using an eccentric-segment geometry increased the effective air-gap flux-density harmonic and simultaneously improved the output characteristics. The reported changes included reductions in cogging torque and torque ripple of 45.5% and 25.7%, respectively, together with a 4.6% increase in output torque [23]. Furthermore, an axial-flux magnetic gear incorporating Halbach-array PMs on its High-Speed Rotor (HSR) was investigated in [24]. The results indicated that an appropriate air-gap arrangement between the HSR magnets can reduce flux leakage and consequently contribute to lower torque ripple.

Despite these developments, achieving high torque capability, low torque ripple, and compact transmission simultaneously remains challenging, particularly for transportation applications such as electric bicycles operating under demanding conditions. To address this challenge, the authors previously introduced a novel Double-Layer Radial-Flux Magnetic Gear (DLRFMG), incorporating two successive torque-conversion stages, in their *ICEMD 2025* conference paper [25]. The HSR, Middle-Speed Rotor (MSR), and Low-Speed Rotor (LSR) employ 4, 9, and 29 pole pairs, respectively, while the inner and outer modulators contain 13 and 38 ferromagnetic pole pieces, resulting in stage transmission ratios of 2.25 and 3.22 and an overall ratio of 5.47. The proposed DLRFMG is optimized using the Taguchi method through a limited number of numerical experiments, considering both maximum applicable torque and torque ripple. The optimized design is subsequently subjected to static structural and modal analyses to evaluate rotor displacement, natural frequencies, and vibration-related behavior. This integrated electromagnetic and structural assessment demonstrates the potential of the proposed configuration to enhance torque-transfer capability and reduce torque pulsations while maintaining satisfactory mechanical performance, providing a promising solution for reliable and low-maintenance magnetic power transmission in transportation and renewable-energy applications.

Building on the work reported in [25], the present manuscript extends the investigation of the proposed DLRFMG by incorporating an additional assessment of its mechanical behavior and vibration characteristics. The magnetic-gear configuration, electromagnetic modeling, and DOE-based optimization procedure, including the L27 Taguchi orthogonal array and ANOVA, follow the approach previously presented in the conference paper, with the corresponding descriptions retained in a slightly more concise form. The main extension of the present study is the evaluation of the mechanical response of the DLRFMG under the electromagnetic forces associated with its initial and optimized configurations. To this end, the radial and tangential electromagnetic force components acting on the three rotors are investigated, followed by static structural analyses to determine their displacement distributions. In addition, modal analysis is conducted to identify the natural frequencies and corresponding mode shapes of the HSR, MSR, and LSR. These additional investigations provide insight into the influence of torque-profile optimization on the mechanical deformation and vibration characteristics of the proposed magnetic gear, thereby extending the scope of [25] beyond electromagnetic performance optimization to include an assessment of its mechanical behavior and structural integrity.

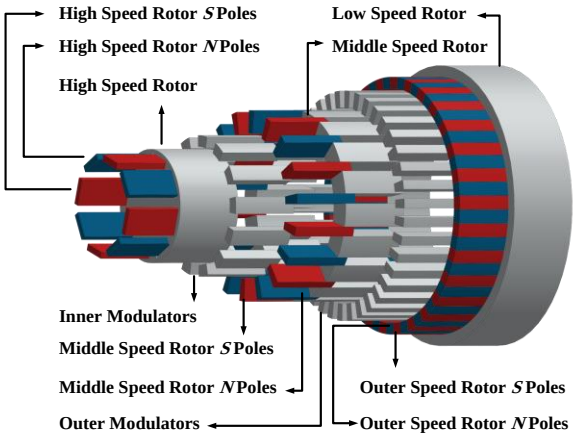


Fig. 1. The proposed double-layer radial-flux magnetic gear (DLRFMG) layout.

2. Operating Principle and The Initial Design Characteristics

2.1. The Proposed Layout and the Operating Principle

The proposed double-layer radial-flux magnetic gear (DLRFMG) operates based on magnetic-field modulation, enabling contactless torque transmission through the interaction of permanent magnets (PMs) and high-permeability ferromagnetic pole pieces. The coaxial configuration comprises five main elements: an inner rotor, inner modulator ring, middle rotor, outer modulator ring, and outer rotor. Different PM topologies are adopted according to the operating requirements: an interior PM (IPM) configuration for the HSR, spoke-type PMs for the MSR, and surface-mounted PMs for the LSR. The modulator rings spatially modulate the magnetic fields generated by the rotors, producing the harmonic components required for synchronous torque transmission. The resulting speed relationship and transmission ratio are determined by the pole-pair numbers of the interacting rotors and the number of ferromagnetic segments in each modulator ring.

TABLE 1. The Initial DLRFMG Design structural parameters values

Parameter	Value
Inner radius of the HSR	10 mm
HSR Thickness	35 mm
HSR PMs thickness	4 mm
HSR PMs length	29 mm
HSR pole-pairs count	4
Air gap	1 mm
Inner modulators thickness	7 mm
Inner modulators pole-pitch	0.5
Inner modulators pole-pieces count	13
MSR PM pole-pitch	0.2
MSR thickness	10 mm
MSR pole-pairs count	9
Outer modulators pole-pitch	0.5
Outer modulators thickness	7 mm
Outer modulators pole-pieces count	38
LSR PMs thickness	4 mm
LSR PMs pole-pitch	0.5
LSR pole-pairs count	29
DLRFMG outer diameter	165 mm
Back-stack length	50 mm

The selection of the PM topologies is also dictated by the mechanical and electromagnetic requirements of each rotor. Surface-mounted PMs on the LSR accommodate its relatively large number of pole pairs, while the spoke-type configuration of the middle rotor supports high torque density. The IPM topology of the HSR enhances mechanical robustness and structural integrity during high-speed operation. The proposed DLRFMG incorporates two consecutive torque-conversion stages: the first comprises the inner rotor, inner modulator ring, and middle rotor, while the second comprises the middle rotor, outer modulator ring, and outer rotor. Accordingly, torque is sequentially transmitted through the two magnetic stages, with the overall transmission ratio determined by the product of the individual stage ratios. Each modulator ring converts the magnetic field of its corresponding rotor into spatial harmonics that interact with the adjacent rotor PMs, as illustrated in Fig. 1.

For proper operation of each modulator ring, its ferromagnetic pole pieces must generate the appropriate spatial harmonic component to establish effective magnetic coupling between the corresponding input and output rotors. Accordingly, the required pole-pair numbers of the rotors and the number of ferromagnetic segments in each modulator ring are determined according to the following relationships:

$$n_{MI} = P_I + P_M = P_I + n_{MO} - P_O \quad (1)$$

$$n_{MO} = P_O + P_M = P_O + n_{MI} - P_I \quad (2)$$

where P_I, P_M, P_O, n_{MO}, and n_{MI} denote the inner rotor (the HSR), middle rotor (the MSR), outer rotor (the LSR) pole-pairs counts, the outer and the inner modulators count, respectively. Consequently, the total and each layer gear ratios, considering the modulators stationary, would be:

$$G_r^{MI} = -\frac{P_M}{P_I} = \frac{P_I - n_{MI}}{P_I} \quad (3)$$

$$G_r^{MO} = -\frac{P_O}{P_M} = \frac{P_M - n_{MO}}{P_M} \quad (4)$$

$$G_r^{Total} = G_r^{MI} G_r^{MO} \quad (5)$$

where G_r^{MI}, G_r^{MO}, and G_r^{Total}, stand for Middle-to-inner stages gear ratio, outer-to-middle stages gear ratio, and the total DLRFMG gear ratio, respectively. The negative sign indicates the direction of rotation for the other rotor is opposite to that of the neighborhood rotor, a common characteristic in magnetic gears due to the flux modulation mechanism. Based on (1) – (5) the rotational velocity of each rotor may be calculated as follows:

$$\omega_I = \frac{P_I - n_{MI}}{n_{MI}}\omega_O + \frac{P_I - n_{MI}}{n_{MI}}\omega_{MI} \quad (6)$$

$$\omega_M = \frac{P_I}{P_I - n_{MI}}\omega_I - \frac{n_{MI}}{P_I - n_{MI}}\omega_{MI} \quad (7)$$

$$\omega_O = \frac{P_M}{P_M - n_{MO}}\omega_M - \frac{n_{MO}}{P_M - n_{MO}}\omega_{MO} \quad (8)$$

where ω_I, ω_M, and ω_O, denote the inner, middle, and outer rotors rotational velocity, respectively. The proposed DLRFMG is optimized to identify a suitable combination of design parameters for improved electromagnetic performance. The initial configuration employs 4, 9, and 29 pole pairs for the HSR, MSR, and LSR, respectively, with 13 and 38 ferromagnetic pole pieces in the inner and outer modulator rings. The principal geometric parameters are given in Table 1. The initial and optimized designs are evaluated using the blocked-rotor and synchronous-speed tests to assess their torque capability and torque transmission performance, respectively.

2.2. The Blocked-Rotor and The Synchronous-Speed Tests

In the proposed DLRFMG, the N42-sintered NdFeB has been utilized as the magnets with the magnetic flux remanence of 1.315 T and 50JN400 non-oriented steel has been used for the HSR, MSR, and LSR iron cores with lamination thickness of 0.5 mm. The blocked-rotor test determines the torque-transfer capability and maximum applicable torque of each component under constrained rotor motion. As shown in Fig. 2, the maximum applicable torques of the HSR, MSR, and LSR are 8.45, 19.02, and 61.26 N·m, respectively, while those of the inner and outer modulator rings are 37.73 and 80.22 N.m. These values define the torque limits of the initial design and serve as references for optimization. Beyond these limits, magnetic synchronism is lost and rotor slip occurs, providing an inherent overload-protection mechanism. The synchronous-speed test evaluates torque transmission under the prescribed speed relationship. The rotors operate at their corresponding synchronous speeds while maintaining the angular reference obtained from the blocked-rotor profile. Proper angular alignment is essential for accurate torque-ripple evaluation, as the initial position directly affects the instantaneous torque and, consequently, the calculated ripple.

Based on Fig. 3, the torque-ripple values of the HSR, MSR, and LSR are 2.055%, 3.83%, and 0.2%, respectively. Although the LSR exhibits low torque ripple, the higher pulsations in the other rotors may increase mechanical vibration, acoustic noise, and dynamic stresses, adversely affecting the efficiency, durability, and long-term reliability of the magnetic gear.

TABLE 2. Control Factors and Their Levels Specification

Control Factors	Label	Level 1	Level 2	Level 3
The HSR PMs thickness	*A*	3.5 mm	4 mm	4.5 mm
The inner modulators thickness	*B*	6 mm	7 mm	8 mm
The outer modulators thickness	*C*	6 mm	7 mm	8 mm
The MSR thickness	*D*	8 mm	10 mm	12 mm
The LSR PMs thickness	*E*	3.5 mm	4 mm	4.5 mm
The inner modulators pole-pitch	*F*	0.45	0.5	0.55
The outer modulators pole-pitch	*G*	0.45	0.5	0.55
The MSR PMs pole-pitch	*H*	0.2	0.3	0.4

TABLE 3. L27 Orthogonal Array of The Proposed DLRFMG

Experiment No.	Control Factors Levels							
	A	*B*	*C*	*D*	*E*	*F*	*G*	*H*
1	3.5	6	6	8	3.5	0.45	0.45	0.2
2	3.5	6	6	8	4.0	0.50	0.50	0.3
3	3.5	6	6	8	4.5	0.55	0.55	0.4
4	3.5	7	7	10	3.5	0.45	0.45	0.3
5	3.5	7	7	10	4.0	0.50	0.50	0.4
6	3.5	7	7	10	4.5	0.55	0.55	0.2
7	3.5	8	8	12	3.5	0.45	0.45	0.4
8	3.5	8	8	12	4.0	0.50	0.50	0.2
9	3.5	8	8	12	4.5	0.55	0.55	0.3
10	4.0	6	7	12	3.5	0.50	0.55	0.2
11	4.0	6	7	12	4.0	0.55	0.45	0.3
12	4.0	6	7	12	4.5	0.45	0.50	0.4
13	4.0	7	8	8	3.5	0.50	0.55	0.3
14	4.0	7	8	8	4.0	0.55	0.45	0.4
15	4.0	7	8	8	4.5	0.45	0.50	0.2
16	4.0	8	6	10	3.5	0.50	0.55	0.4
17	4.0	8	6	10	4.0	0.55	0.45	0.2
18	4.0	8	6	10	4.5	0.45	0.50	0.3
19	4.5	6	8	10	3.5	0.55	0.50	0.2
20	4.5	6	8	10	4.0	0.45	0.55	0.3
21	4.5	6	8	10	4.5	0.50	0.45	0.4
22	4.5	7	6	12	3.5	0.55	0.50	0.3
23	4.5	7	6	12	4.0	0.45	0.55	0.4
24	4.5	7	6	12	4.5	0.50	0.45	0.2
25	4.5	8	7	8	3.5	0.55	0.50	0.4
26	4.5	8	7	8	4.0	0.45	0.55	0.2
27	4.5	8	7	8	4.5	0.50	0.45	0.3

TABLE 4. The Material and Mesh Properties of the Proposed DLRFMG

Control Factors	Dimension
Magnets maximum mesh size	0.75 mm
Modulators and MSR iron core maximum mesh size	0.7 mm
LSR and HSR iron cores maximum mesh size	1 mm
Boundaries maximum mesh size	0.7 mm
Total layout minimum mesh size	0.155 mm
Total layout maximum mesh size	1 mm
Total layout average mesh size	0.684 mm

It needs to be mentioned that the material and mesh properties of the under study DLRFMG are given in Table 4. It has been made sure the appropriate mesh has been generated to achieve high calculation precision. On this matter, the convergence tolerance and maximum iterations count have been set on 10^{-8} and 5000, respectively.

3. TAGUCHI OPTIMIZATION PROCEDURE

The Taguchi design of experiments provides a systematic approach for evaluating the effects of multiple design variables while substantially reducing the required numerical trials through orthogonal arrays. For the proposed DLRFMG, an L27 orthogonal array with three levels for each of the eight control factors is employed. A full-factorial design would require $3^8 = 6561$ cases, whereas the Taguchi method reduces this to only 27 strategically selected simulations, significantly improving computational efficiency while enabling the principal effects of the design variables to be identified. The complete experimental matrix and factor levels are presented in Tables 2 and 3. These parameters represent the principal geometric variables of the proposed magnetic gear and their ranges are selected according to the initial design configuration, practical geometric limitations, and the design requirements of the DLRFMG.

The optimization results are evaluated using signal-to-noise (S/N) ratios analysis and analysis of variance (ANOVA). The S/N ratios analysis is used to identify the favorable level of each control factor according to the optimization objective, while ANOVA quantifies the relative contribution and statistical significance of the factors. These methods are subsequently employed to determine the parameter combination corresponding to the optimized DLRFMG configuration.

3.1. S/N Ratios Analysis

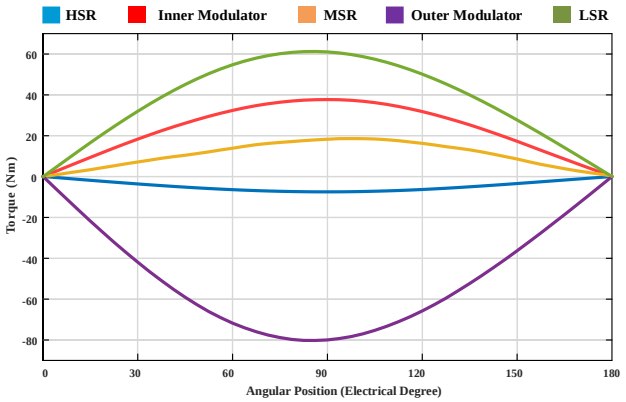


Fig. 2. The DLRFMG blocked-rotor test characteristic.

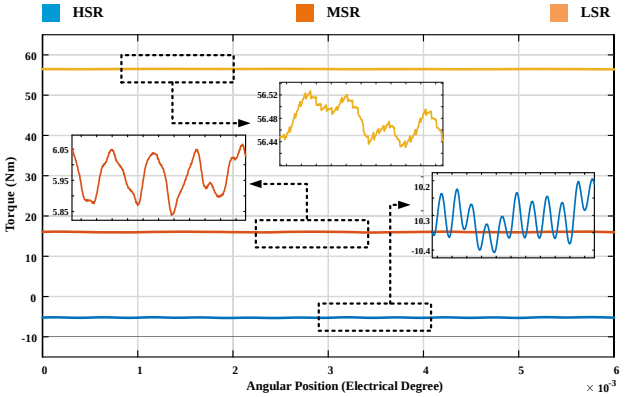


Fig. 3. The DLRFMG synchronous-speed test characteristic.

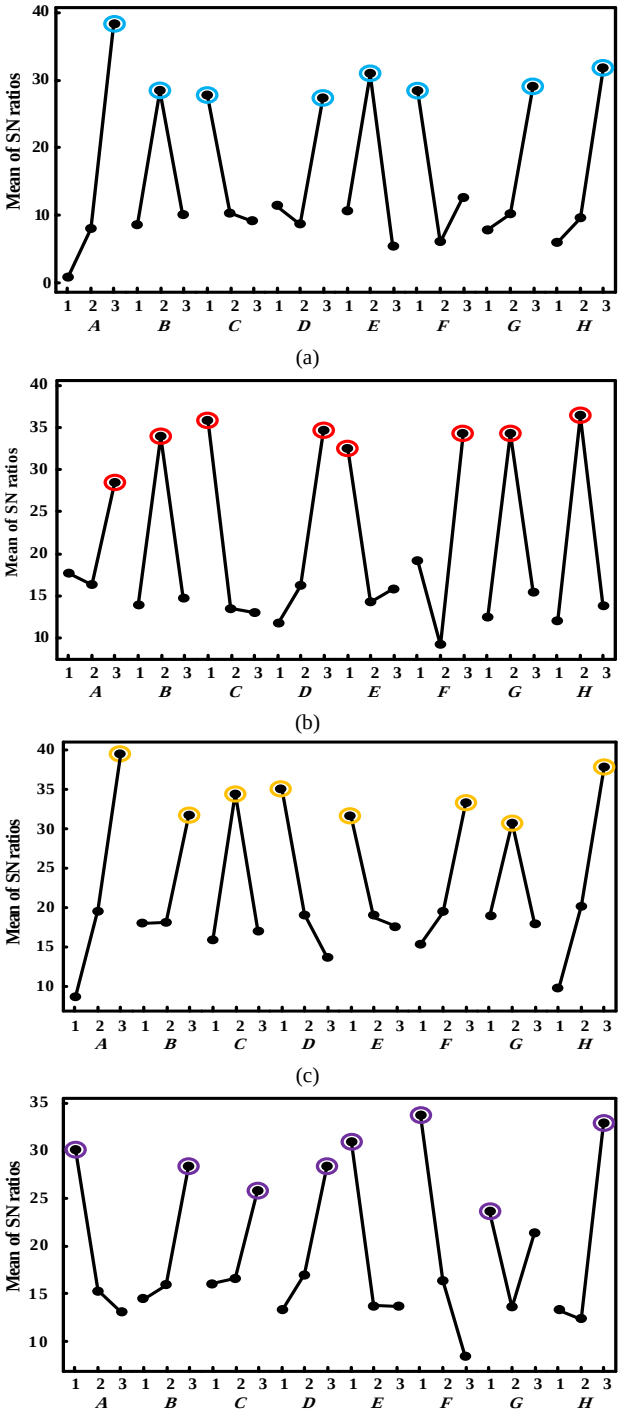


Fig. 4. The S/N ratios of (a) the MSR maximum applicable torque (b) the HSR torque ripple (c) the MSR torque ripple (d) and the LSR torque ripple.

Within the Taguchi framework, the S/N ratios evaluates the quality and robustness of an optimized response by relating the desired performance to undesirable variations. A higher S/N ratio generally indicates improved performance with greater resistance to variation, enabling the identification of favorable and robust factor levels. Three standard S/N criteria are available: "larger-is-better" for maximizing the response, "smaller-is-better" for minimizing it, and "nominal-is-the-best" when the response should approach a specified target. Accordingly, the appropriate criterion is selected based on the optimization objective of each response.

It should also be noted that the normalization procedure must be selected consistently with the adopted S/N criterion. Since different response objectives require different formulations, the corresponding mean-square deviation (MSD) expressions are first determined and subsequently used to calculate the appropriate S/N ratios. The MSD formulations associated with the three S/N criteria considered in the Taguchi methodology are given below [26]:

The larger-is-better:

$$MSD_N = \sum_{i=1}^{n} \frac{\frac{1}{y_i^2}}{n} \tag{9}$$

The smaller-is-better:

$$MSD_L = \sum_{i=1}^{n} \frac{y_i^2}{n} \tag{10}$$

The nominal-is-the-best:

$$MSD_S = \sum_{i=1}^{n} \frac{(y_i - m)^2}{n} \tag{11}$$

The Taguchi optimization considers four responses: maximum applicable torque and torque ripple of the HSR, MSR, and LSR. The maximum applicable torque is optimized for the MSR only, since the torque limits of the other rotors are determined by the prescribed gear ratios, whereas torque ripple varies independently among the rotors and is therefore treated separately.

The S/N ratios for the four responses are presented in Fig. 4 and Tables 5–8. The highest S/N ratio determines the preferred level of each factor, while the max–min difference is used to rank the relative influence of the factors on each response. The resulting optimum level sequences for factors A–H are 3-2-1-3-2-1-3-3 for maximum applicable torque, 3-2-1-3-1-3-2-2 for HSR torque ripple, 3-3-2-1-1-3-2-3 for MSR torque ripple, and 1-3-3-3-1-1-1-3 for LSR torque ripple. The relative influence of the design variables varies depending on the selected performance response. For the maximum applicable torque of the MSR, the HSR PM thickness, MSR PM pole-pitch, and LSR PM thickness are identified as the three most influential parameters. In terms of HSR torque ripple, the dominant parameters are the pole-pitch of the inner modulator, the MSR PM pole-pitch, and the MSR thickness. The HSR PM thickness, MSR PM pole-pitch, and MSR thickness exhibit the greatest influence on the MSR torque ripple. For the LSR torque ripple, the inner-modulator pole-pitch, MSR PM pole-pitch, and LSR PM thickness are found to be the most significant factors. These results demonstrate that the relative importance of a given geometric parameter depends strongly on the performance criterion being optimized.

Since the individual responses yield different optimal factor combinations, a weighted Multi-Objective Function (MOF) is employed to obtain a single overall optimum. Greater emphasis is assigned to maximum applicable torque due to the relatively small numerical magnitude of torque ripple, with weighting coefficients of 0.70, 0.05, 0.20, and 0.05 for the MSR maximum applicable torque, HSR torque ripple, MSR torque ripple, and LSR torque ripple, respectively.

The S/N ratios obtained from the resulting multi-objective formulation are presented in Fig. 5 and Table 9. These results provide a unified basis for determining the combination of control-factor levels that offers the most favorable compromise among the considered performance requirements. The mathematical expression used to construct the Multi-Objective Function (MOF) is given below:

$$MOF = k_1 MaxT_{MSR} + k_2 T_{HSR}^{Ripple} + k_3 T_{MSR}^{Ripple} + k_4 T_{LSR}^{Ripple} \quad (10)$$

In multi-objective optimization problems, either the smaller-is-better or the larger-is-better criterion can be adopted, provided that the normalization procedure is appropriately selected according to the desired optimization direction. When the smaller-is-better criterion is employed, the normalization should assign a value of zero to the best response and a value of one to the worst response. Conversely, for the larger-is-better criterion, the best and worst responses should be assigned values of one and zero, respectively. In the present study, the smaller-is-better criterion is adopted for the combined multi-objective optimization. Accordingly, the torque-ripple responses are normalized directly, such that lower ripple values correspond to lower normalized values. In contrast, the maximum applicable torque is normalized inversely, ensuring that higher torque values result in lower normalized values. This approach converts all individual objectives into a common minimization framework, allowing them to be consistently combined within the multi-objective function. Based on our previous experience with multi-objective optimization of magnetic gears, particularly in problems involving torque-ripple reduction, adopting a common smaller-is-better formulation has been found to provide a more consistent optimization procedure and reduce the likelihood of errors associated with handling different optimization directions.

According to the normalization procedure defined below in Eq. (12), the best-performing response is assigned a normalized value of zero, whereas the worst-performing response is assigned a value of one. The normalized values of the remaining responses are distributed within the range of zero to one, depending on their relative performance.

$$Output_{norm} = \frac{|Output - BestOutput|}{MaxOutput - MinOutput} \quad (12)$$

As shown in Fig. 5, the combined multi-objective analysis identifies the third, second, first, first, second, first, third, and third levels as the optimum settings for control factors A–H, respectively. These level selections represent the best overall compromise among the considered torque-performance objectives. Based on the corresponding influence analysis, the HSR PM thickness, LSR PM thickness, and MSR PM pole-pitch are identified as the three most influential design parameters governing the overall optimization response.

TABLE 5. The MSR Maximum Applicable Torque S/N Ratios Results

Level	A	B	C	D	E	F	G	H
1	0.89	8.5173	27.69	11.27	10.79	28.3	7.84	6.01
2	8.02	28.3318	10.3	8.58	30.8	6.02	10.17	9.61
3	38.10	10.1787	9.03	27.17	5.43	12.7	29	31.40
Max-Min Difference	37.20	19.8144	18.66	18.59	25.36	22.28	21.16	25.39
Rank	1	6	7	8	3	4	5	2

TABLE 6. The HSR Torque Ripple S/N Ratios Analysis Results

Level	A	B	C	D	E	F	G	H
1	17.63	13.84	35.78	11.7	32.39	19.15	12.47	12.03
2	16.29	33.93	13.52	16.15	14.16	9.1	34.31	36.44
3	28.41	14.56	13.03	34.48	15.78	34.08	15.55	13.86
Max-Min Difference	12.11	20.08	22.74	22.79	18.22	24.97	21.83	24.41
Rank	8	6	4	3	7	1	5	2

TABLE 7. The MSR Torque Ripple S/N Ratios Analysis Results

Level	A	B	C	D	E	F	G	H
1	8.7	18.02	15.94	34.89	31.37	15.32	18.96	9.87
2	19.76	18.13	34.55	19.07	18.78	19.31	30.72	20.27
3	39.25	31.55	17.22	13.73	17.54	33.06	18.01	37.55
Max-Min Difference	30.54	13.53	18.61	21.16	13.83	17.73	12.7	27.68
Rank	1	7	4	3	6	5	8	2

TABLE 8. The LSR Torque Ripple S/N Ratios Analysis Results

Level	A	B	C	D	E	F	G	H
1	29.99	14.38	16.08	13.18	30.99	33.68	23.55	13.26
2	15.34	15.85	16.58	16.98	13.78	16.38	13.58	12.31
3	13.12	28.21	25.8	28.29	13.7	8.4	21.34	32.89
Max-Min Difference	16.87	13.82	9.72	15.11	17.29	25.28	9.97	20.58
Rank	4	6	8	5	3	1	7	2

3.2. The ANOVA Analysis

ANOVA is employed to quantify the relative contribution of the eight control factors to each performance response using the Sum of Squares (SS), F-value, P-value, and Participation Percentage (PP). At a 95% confidence level, factors with $P < 0.05$ are considered statistically significant. Since each factor has three levels, each contributes two degrees of freedom, giving 16 DOF for the eight factors, with the remaining DOF assigned to residual error. The ANOVA results for the individual responses and the weighted multi-objective function are presented in Tables 10 and 11, respectively.

TABLE 9. The Multi-Objective Function S/N Ratios Analysis Results

Level	A	B	C	D	E	F	G	H
1	2.68	9.55	11.13	10.64	10.18	11.68	8.7	6.84
2	9.54	11.79	9.91	9.67	13.59	7.5	9.59	10.63
3	18.56	9.43	9.73	10.46	7	11.59	12.48	13.29
Max-Min Difference	15.88	2.36	1.39	0.96	6.59	4.18	3.78	6.45
Rank	1	6	7	8	2	4	5	3

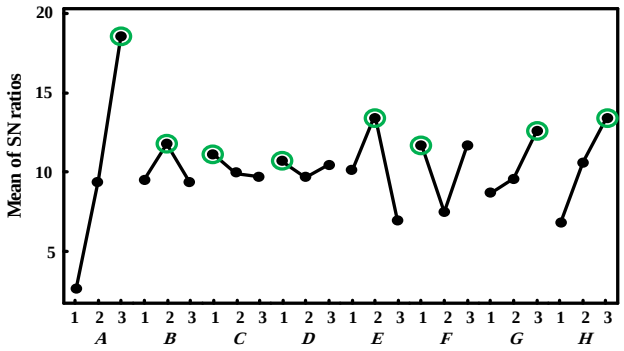


Fig. 5. The S/N ratios of the multi-objective optimization function.

For the MSR maximum applicable torque, HSR PM thickness is dominant with an 86.78% contribution. For HSR torque ripple, the inner-modulator pole-pitch and HSR PM thickness contribute 32.37% and 23.57%, respectively, while HSR PM thickness and MSR PM pole-pitch dominate the MSR torque ripple with contributions of 46.22% and 23.47%. For LSR torque ripple, the inner- and outer-modulator pole-pitches are the most influential factors, contributing 41.67% and 26%, respectively. In the combined optimization, HSR PM thickness remains dominant, accounting for 83.62% of the total variation.

The residual errors for the MSR maximum applicable torque, HSR torque ripple, MSR torque ripple, LSR torque ripple, and multi-objective function are 0.82%, 7.78%, 6.99%, 6.41%, and 0.42%, respectively, indicating that the selected factors explain most of the response variation and confirming the effectiveness of the Taguchi-based optimization.

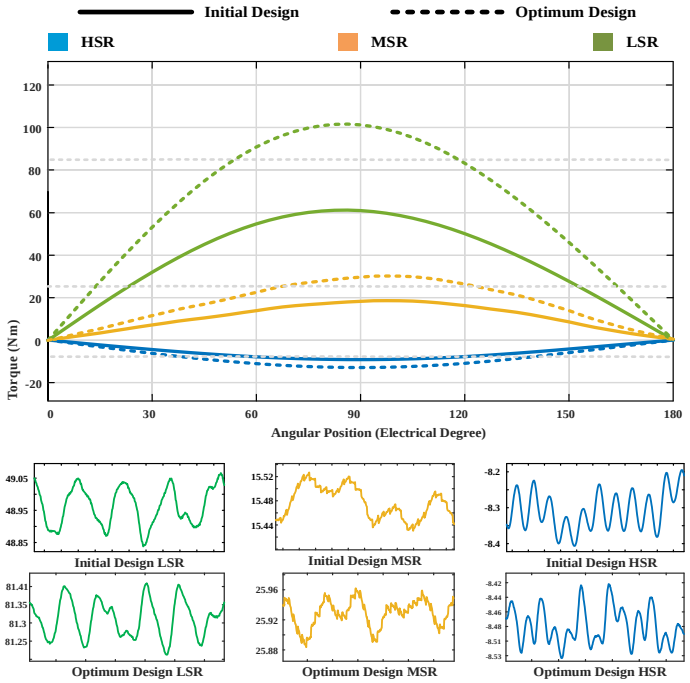


Fig. 6. The DLRFMG blocked-rotor and synchronous-speed tests characteristics of both initial and optimum designs.

4. The Initial and The Optimum Designs Comparison

Comparison of the initial and optimized DLRFMG configurations confirms the effectiveness of the Taguchi-based optimization. The optimum levels of factors A–H are 3, 2, 1, 1, 2, 1, 3, and 3, respectively, with HSR PM thickness identified by ANOVA as the dominant parameter. Notably, this optimum combination is not included among the original L27 cases, demonstrating the ability of the Taguchi method to predict an improved configuration beyond the explicitly simulated designs.

As shown in Fig. 6, the optimized DLRFMG achieves maximum applicable torques of 11.62, 31.71, and 102.11 N·m for the HSR, MSR, and LSR, respectively, with stage and overall transmission ratios of 2.25, 3.22, and 5.47. Compared with the initial design, these values represent torque-capability improvements of 37.51%, 66.71%, and 66.68%, respectively. The corresponding

TABLE 10. ANOVA Results of The Proposed DLRFMG Objectives.

Factors	DOF	MSR Maximum Applicable Torque				HSR Torque Ripple				MSR Torque Ripple				LSR Torque Ripple			
		SS	P (%)	F	P	SS	P (%)	F	P	SS	P (%)	F	P	SS	P(%)	F	P
A	2	2.489	86.78	572.43	4.87×10^{-11}	0.26914	23.57	15.17	9.37×10^{-4}	0.70974	46.22	33.06	3.91×10^{-5}	0.13194	9.21	7.17	0.0117
B	2	0.009	0.31	2.27	0.154	0.04306	3.77	2.43	0.1383	0.08098	5.27	3.77	0.06016	0.02586	1.81	1.41	0.2899
C	2	0.005	0.17	1.08	0.378	0.08649	7.57	4.87	0.0333	0.09986	6.5	4.65	0.03731	0.02670	1.86	1.45	0.2798
D	2	0.022	0.77	5.07	0.030	0.10490	9.19	5.91	0.0202	0.12556	8.18	5.85	0.02079	0.00182	0.13	0.10	0.9068
E	2	0.139	4.84	32.11	4.4×10^{-5}	0.04214	3.69	2.37	0.1433	0.00798	0.52	0.37	0.69877	0.11219	7.83	6.10	0.0186
F	2	0.086	3	19.77	3.35×10^{-4}	0.36951	32.37	20.82	0.0003	0.01914	1.25	0.89	0.44019	0.59696	41.67	32.44	4.3×10^{-5}
G	2	0.016	0.56	3.60	0.067	0.12639	11.07	7.12	0.0119	0.02457	1.6	1.14	0.35674	0.37247	26	20.24	3.1×10^{-4}
H	2	0.079	2.75	18.27	4.58×10^{-4}	0.01132	0.99	0.64	0.5486	0.36033	23.47	16.79	6.3×10^{-4}	0.07278	5.08	3.95	0.0543
Error	10	0.022	0.82	-	-	0.08872	7.78	-	-	0.10734	6.99	-	-	0.09202	6.41	-	-
Total	26	2.868	100	-	-	1.14167	100	-	-	1.53549	100	-	-	1.43274	100	-	-

torque-ripple values decrease to 0.52%, 1.37%, and 0.08%, representing reductions of 74.69%, 64.23%, and 60% for the HSR, MSR, and LSR. Thus, the optimized configuration simultaneously enhances torque-transfer capability and suppresses torque pulsations, while its magnetic flux-density distribution is further examined in Fig. 7.

5. Structural Analysis

Reducing torque ripple is essential for improving the mechanical performance, stability, and reliability of magnetic gear systems, as excessive torque fluctuations can induce undesirable mechanical vibrations, dynamic stresses, and fatigue-related issues. Therefore, following the optimization of maximum applicable torque and torque ripple, a structural analysis is performed to evaluate the mechanical characteristics of the proposed magnetic gear. In this regard, the structural analysis focuses on the displacement analysis and modal shapes of the proposed structure to ensure that the optimized electromagnetic performance is achieved without compromising its mechanical integrity. Through the optimization procedure, the maximum applicable torque to the HSR, MSR, and LSR have been improved for 37.51%, 66.71%, and 66.68%, while the torque ripples are attenuated for 74.69%, 64.23%, and 60%, respectively. Thus, it is worthy to ensure that the mechanical characteristics maintain appropriate values. The mechanical properties of the materials used in the structural and modal analyses are summarized in Table 12. These properties include density, Young's modulus, shear modulus, and Poisson's ratio for the 50JN400 non-oriented electrical steel used in the rotor cores and the N42 sintered NdFeB permanent magnets. The corresponding material properties were assigned to the respective components in the finite-element model to evaluate their mechanical deformation and modal characteristics.

5.1. Displacement Analysis

The displacement of a magnetic device components is affected by the magnetic forces interactions. In accordance with the coaxial layout of the proposed DLRFMG the axial magnetic force component is zero. Thus, the magnetic force is composed of radial and tangential components, which may be expressed as follows:

$$F_r = \frac{1}{2\mu_0}\left(B_r^2 - B_\theta^2\right) \tag{10}$$

$$F_\theta = \frac{B_r B_\theta}{\mu_0} \tag{11}$$

Where B_r, B_θ, μ_0, F_r, and F_θ denotes the radial and tangential flux densities, air permeability, and the radial and tangential magnetic forces.

The radial and tangential magnetic force waveforms of the initial and optimized designs are presented in Fig. 8, where solid and dotted lines represent the initial and optimized designs, respectively. As it may be observed, both designs exhibit a similar overall force-waveform pattern. Nevertheless, the optimized design demonstrates higher tangential force magnitudes across all three rotors, thereby contributing to the enhanced torque capability of the proposed structure. It can also be observed that the radial and tangential forces acting on the MSR exhibit pronounced peaks at specific rotor positions. These sharp variations are primarily attributed to localized magnetic-flux saturation at the edges of the inner modulators. Furthermore, the absolute values of the radial and tangential forces in the MSR and LSR remain below approximately 3 N, whereas those in the HSR can reach nearly 36 N. In general, owing to the multiple interleaved rotating and stationary components in the proposed DLRFMG, the magnitude of the radial force alone cannot be directly correlated with the severity of the resulting displacement or vibration. Therefore, a static structural analysis is performed for both the initial and optimized designs to quantitatively

TABLE 11. The ANOVA Results Of The Multi-Objective Function

Factors	DOF	SS	P (%)	F	P
A	2	1.51414	83.62	981.70	3.34×10^{-12}
B	2	0.02001	1.11	12.98	0.0016
C	2	0.00980	0.54	6.35	0.0165
D	2	0.02359	1.31	15.30	0.0009
E	2	0.06506	3.59	42.18	1.34×10^{-5}
F	2	0.04446	2.45	28.83	7.05×10^{-5}
G	2	0.01719	0.95	11.15	0.0028
H	2	0.10884	6.01	70.57	1.2×10^{-6}
Error	10	0.00771	0.42	-	-
Total	26	1.81081	100	-	-

TABLE 12. Mechanical Properties of 50JN400 Electrical Steel and N42 NdFeB Permanent Magnets

Material	Property	Value
50JN400 non-oriented steel	Density (kg/m3)	7650
	Young Modulus (GPa)	200
	Shear Modulus (G)	76.92
	Poisson Ratio	0.3
NdFeB – N42	Density (kg/m3)	7500
	Young Modulus (GPa)	160
	Shear Modulus (G)	64.52
	Poisson Ratio	0.24

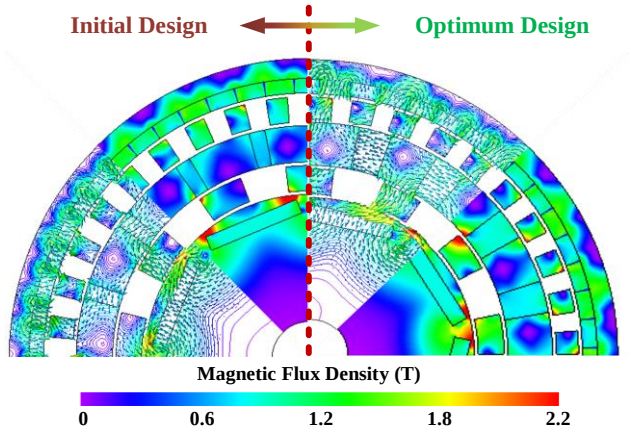


Fig. 7. The magnetic flux density of the both initial and optimum designs.

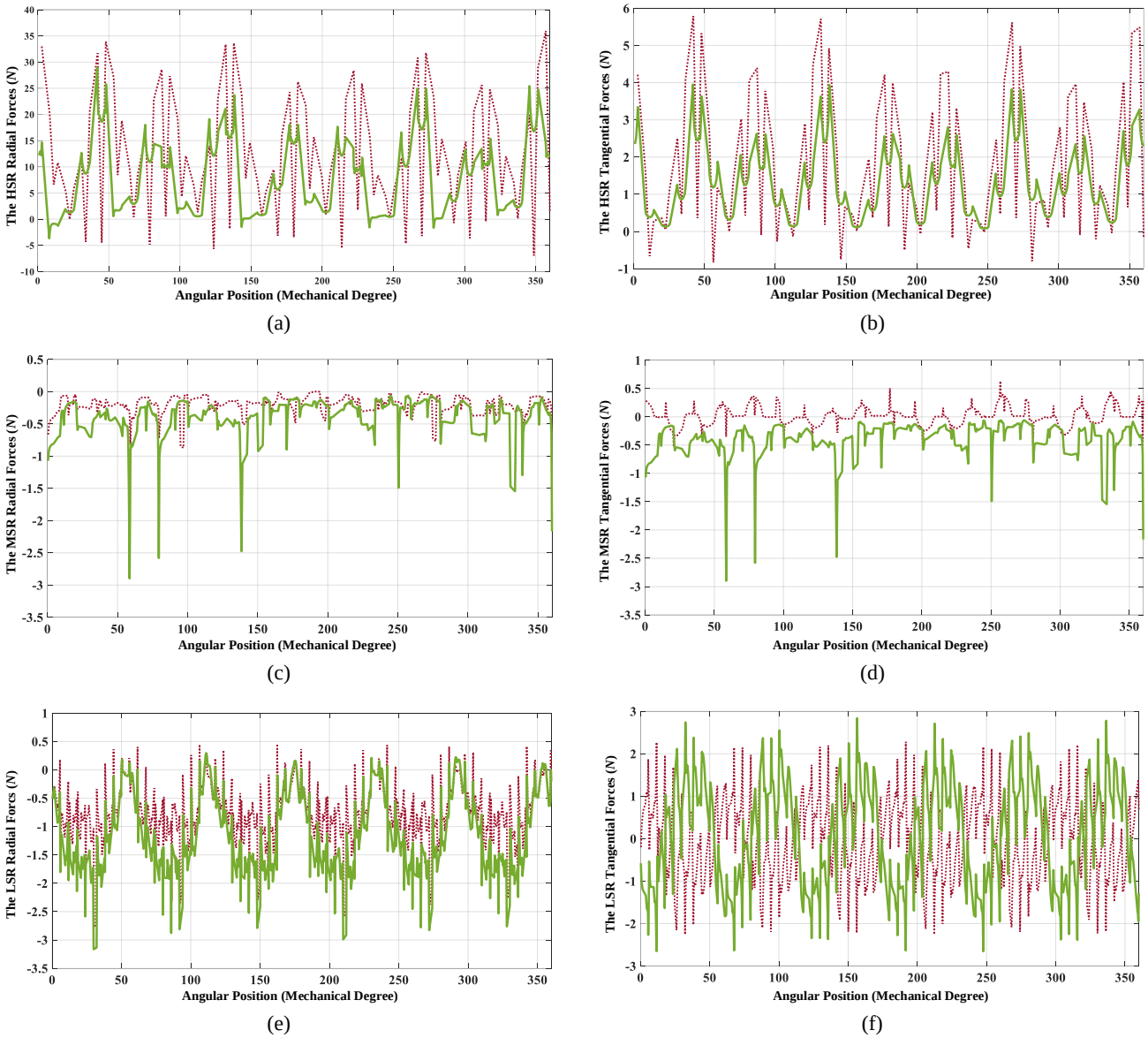
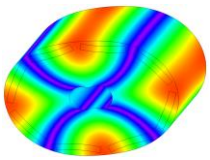
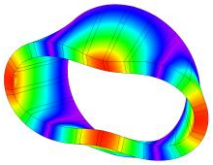
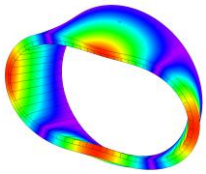
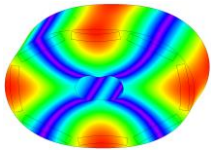
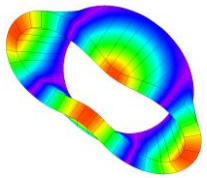
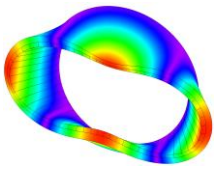
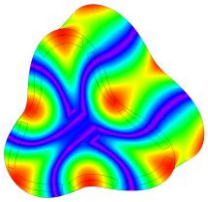
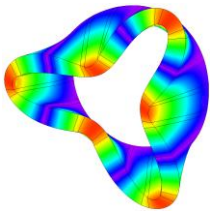
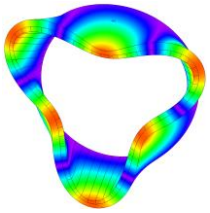
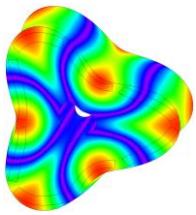
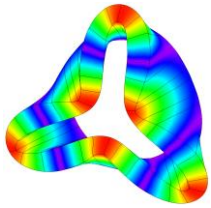
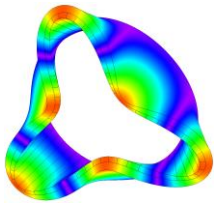
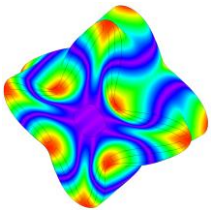
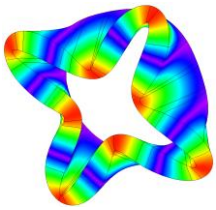
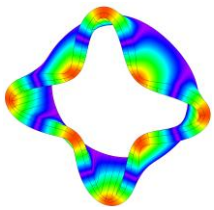
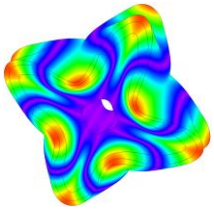
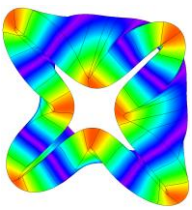
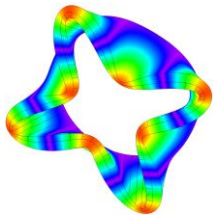


Fig. 8. (a) the HSR radial forces, (b) the HSR tangential forces, (c) the MSR radial forces, (d) the MSR tangential forces, (e) the LSR radial forces, and (f) the LSR tangential forces of both initial and optimum designs.

evaluate their mechanical displacements and assess the structural response under the magnetic forces.

The static structural analysis was performed for all three rotors, and the corresponding displacement distributions are presented in Figs. 9–11. Owing to the coaxial configuration of the proposed DLRFMG, the HSR exhibits greater structural robustness, as its inner shaft is fully supported and the permanent magnets (PMs) are located internally. As shown in Fig. 9, the maximum displacement of the HSR occurs near the end edges of the PMs, reaching 6.4 and 10 μm for the initial and optimum designs, respectively. Nevertheless, the average displacement remains relatively low, at approximately 3.5 and 5.3 μm for the initial and optimized optimum, respectively. In contrast, the MSR and LSR are supported from only one side, resulting in lower structural stiffness and consequently larger displacements than that of the HSR, as it would be observed in Figs (10) and (11). For the MSR, the maximum displacement increases from 28 μm in the initial design to 36 μm in the optimum design, while the corresponding average displacement increases from 14.5 to 18.3 μm. Similarly, the maximum displacement of the LSR is 60 and 55 μm for the initial and optimum designs, respectively, whereas the corresponding average displacement decreases from 27.2 to 25.9 μm. According to IEC 60034-14:2026, the mounting conditions and vibration severity of rotating electrical machines are classified to establish consistent criteria for vibration measurement and evaluation. The standard defines two vibration severity grades: Grade A, which applies to machines without special vibration requirements, and Grade B, which applies to machines subject to more stringent vibration requirements. Furthermore, the standard distinguishes between two principal

TABLE 14. The Second, Third, and the Fourth Vibration Modes and Their Natural Frequencies

Mode Order	Initial Design Mode Shapes and Natural Frequencies			Optimum Design Mode Shapes and Natural Frequencies		
	HSR	MSR	LSR	HSR	MSR	LSR
2	 28690 Hz	 7146 Hz	 6346 Hz	 29416 Hz	 7310 Hz	 6346 Hz
3	 41086 Hz	 8255 Hz	 6443 Hz	 42964 Hz	 8974 Hz	 6443 Hz
4	 52086 Hz	 11631 Hz	 7782 Hz	 52988 Hz	 12907 Hz	 7782 Hz

mounting arrangements: free suspension and rigid mounting. In the free-suspension condition, the machine is supported by elastic elements, such as springs or rubber mounts, to minimize the influence of the supporting structure on its vibration response. In contrast, rigid mounting involves securely fastening the machine to a massive foundation or a sufficiently stiff test stand, thereby providing stable mechanical support during vibration measurements.

Based on the obtained static structural results, the maximum displacements of the optimized HSR, MSR, and LSR are 10, 28, and 55 μm, respectively. These values indicate that the structural deformations remain relatively limited compared with the nominal air-gap dimension of 1 mm. Therefore, the proposed DLRFMG satisfies the displacement-related mechanical design considerations adopted in this study. It should be noted that this assessment concerns static structural deformation and does not, by itself, establish formal compliance with the vibration severity limits of IEC 60034-14. The corresponding displacement limits of IEC-60034-14 are given in Table 13.

The mechanical integrity of the proposed DLRFMG was further evaluated through static structural and modal analyses. The maximum von Mises stress obtained for the 50JN400 electrical steel was 152.5 MPa. Based on the mechanical properties assigned to the material, the corresponding safety factor was calculated to be 2.05.

TABLE 13. IEC-60034-14 Requirements [27]

Vibration Grade	Shaft height (mm)	56 ≤ H ≤ 132	132 ≤ H
	Mounting	Displacement (μm)	Displacement (μm)
A	Free suspension	45	48
	Rigid mounting	-	37
B	Free suspension	18	29
	Rigid mounting	-	24

A comparison of Fig. 8 with Figs. 9–11 further reveals a strong correlation between the electromagnetic force distributions and the resulting structural deformation. Owing to the periodic nature of the radial and tangential force waveforms of the HSR and LSR, the displacement distributions on the HSR surface and the free side of the LSR also exhibit a periodic pattern. In particular, the displacement distribution of the LSR forms a pattern resembling a hexagonal configuration. In contrast, the radial and tangential forces acting on the MSR exhibit sharp increases at specific angular positions, resulting in localized deformation and a predominantly non-periodic displacement distribution. Overall, the optimization leads to an increase of 53.84% and 28.57% in the maximum displacement of the HSR and MSR, respectively, whereas the maximum displacement of the LSR decreases by 8.33%. Despite these variations, the obtained displacement levels remain within the acceptable structural limits of the proposed DLRFMG.

5.2. Modal Shapes

Following the static structural analysis, modal analysis is performed to determine the natural frequencies and corresponding mode shapes of the rotors in the proposed DLRFMG. The identification of the natural frequencies is essential for evaluating the potential resonance conditions of the magnetic device during operation. In particular, the periodic electromagnetic forces and torque pulsations generated during

operation can excite the structural modes of the rotors. Therefore, the operating speed and excitation frequencies should be selected such that they remain sufficiently separated from the natural frequencies of the structure, thereby avoiding resonance and the associated excessive vibration. Accordingly, the modal characteristics of the HSR, MSR, and LSR are investigated to identify their critical natural frequencies, as given in Table 14.

It can be observed that the second-mode natural frequencies of the HSR, MSR, and LSR are 29416, 7310, and 6346 Hz, respectively. For the third-mode, the corresponding natural frequencies are 42964, 8974, and 6443 Hz, while those of the fourth-mode are 52988, 12907, and 7782 Hz, respectively, for the optimized design. For the initial design, the natural frequencies associated with the second mode are 2869, 7146, and 6346 Hz for the HSR, MSR, and LSR, respectively. The corresponding values for the third mode are 41086, 8255, and 6443 Hz, whereas the fourth-mode natural frequencies are 52086, 11631, and 7782 Hz, respectively.

The frequency difference between the modal shapes is considerably greater for the HSR. This can be attributed to the distinct mechanical configurations of the three rotors. Specifically, the MSR and LSR are supported from only one side, resulting in comparatively lower mechanical stiffness and stability. In contrast, the shaft is positioned within the HSR and provides enhanced mechanical support and structural rigidity. Consequently, the HSR exhibits substantially higher natural frequencies across its corresponding modal shapes. Furthermore, the slight increase in resonance frequencies confirms that the torque-profile optimization improves performance while maintaining acceptable displacement and vibration levels.

6. Conclusion

This paper introduced and optimized a novel double-layer radial-flux magnetic gear (DLRFMG) to enhance torque transmission capability and reduce torque ripple using the Taguchi optimization method. The proposed configuration effectively exploits magnetic flux modulation through a successive torque-conversion stage, enabling high torque transmission. The optimization results demonstrated a substantial improvement over the initial design. Specifically, the maximum applicable torques of the HSR, MSR, and LSR were increased by 37.51%, 66.71%, and 66.68%, respectively, while their torque ripples were reduced by 74.69%, 64.23%, and 60.00%, respectively. These results demonstrate the effectiveness of the Taguchi method in identifying favorable geometrical parameters with a significantly reduced number of simulations compared with a full-factorial design. The ANOVA results further revealed that the HSR PM thickness is the most influential parameter, contributing 83.62% to the overall performance. Furthermore, static structural and modal analyses were conducted to assess the mechanical behavior of the optimized DLRFMG under the enhanced torque conditions. The displacement analysis showed that, although the maximum displacements of the HSR and MSR increased by 53.84% and 28.57%, respectively, the maximum displacement of the LSR decreased by 8.33%. The obtained displacement levels remain within acceptable limits, indicating that the substantial improvement in torque capability does not compromise the structural integrity of the proposed magnetic gear. In addition, the modal analysis confirmed sufficiently high natural frequencies for all three rotors, with the HSR exhibiting considerably higher modal frequencies owing to its greater mechanical support and structural rigidity. Overall, the combined electromagnetic and structural analyses demonstrate that the optimized DLRFMG achieves significantly enhanced torque performance and reduced torque ripple while maintaining satisfactory mechanical stability and vibration characteristics,

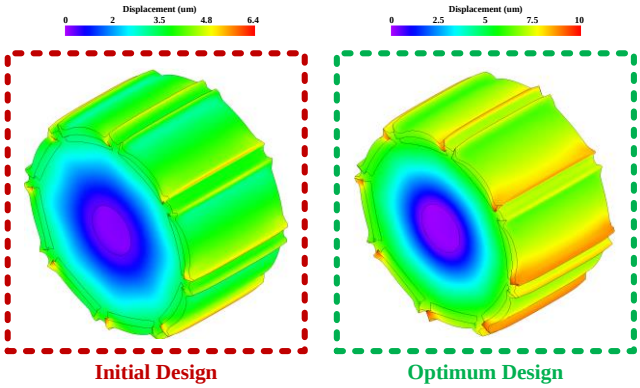


Fig. 9. The displacement distribution of the HSR for both initial and optimum designs.

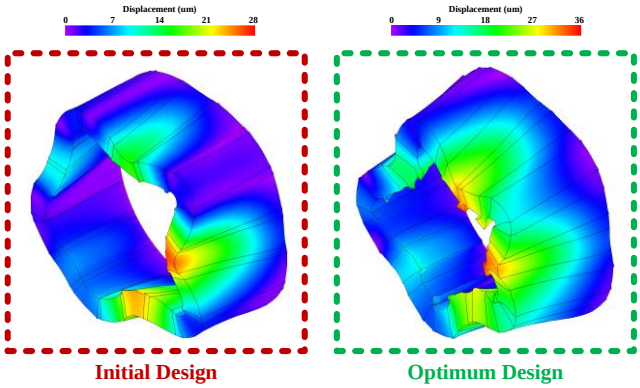


Fig. 10. The displacement distribution of the MSR for both initial and optimum designs.

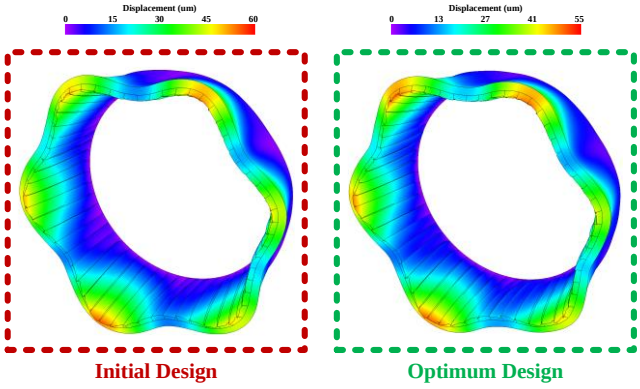


Fig. 11. The displacement distribution of the LSR for both initial and optimum designs.

highlighting its potential for high-performance applications in electric transportation and other advanced energy systems.

REFERENCES

[1] F. A. Machado, P. J. Kollmeyer, D. G. Barroso, and A. Emadi, "Multi-speed gearboxes for battery electric vehicles: Current status and future trends," *IEEE Open Journal of Vehicular Technology*, vol. 2, pp. 419-435, 2021.

[2] A. Darabi, M. Abolghasemi, R. Mirzahosseini and M. Sarvi-Maraghi, "Transient Analysis of an Axial Flux Magnetic Gear," *28th Iranian Conference on Electrical Engineering (ICEE)*, pp. 1-5, 2020.

[3] B. McGilton, R. Crozier, A. McDonald, and M. Mueller, "Review of magnetic gear technologies and their applications in marine energy," *IET Renewable Power Generation*, vol. 12, no. 2, pp. 174-181, 2018.

[4] A. Zarghani, A. Ghaheri, M. Abolghasemi, E. Afjei and H. Torkaman, "Thermal Modeling and Analysis of Transverse-Radial Flux Magnetic Gear," *3rd International Conference on Electrical Machines and Drives (ICEMD)*, pp. 1-7, 2023.

[5] C. G. Armstrong, "Power transmitting device," US Pat. 687 292, 1901

[6] H. T. Faus, "Magnet gearing," US Pat. 2 243 555, 1941

[7] N. W. Frank and H. A. Toliyat, "Analysis of the concentric planetary magnetic gear with strengthened stator and interior permanent magnet inner rotor," *IEEE transactions on industry applications*, vol. 47, no. 4, pp. 1652-1660, 2011.

[8] B. Dai, K. Nakamura, Y. Suzuki, Y. Tachiya, and K. Kuritani, "Comparison of two different interior permanent magnet type low-speed rotor structures of axial-flux magnetic gear," *IEEJ Journal of Industry Applications*, vol. 10, no. 6, pp. 632-637, 2021.

[9] P. Tlali, R. Wang, and S. Gerber, "Magnetic gear technologies: A review," *International Conference on Electrical Machines (ICEM)*, pp. 544-550, 2014.

[10] K. Atallah and D. Howe, "A novel high-performance magnetic gear," *IEEE Transactions on Magnetics*, vol. 37, no. 4, pp. 2844–2846, 2001.

[11] B. Praslicka, M. C. Gardner, M. Johnson, and H. A. Toliyat, "Review and analysis of coaxial magnetic gear pole pair count selection effects," *IEEE Journal of Emerging and Selected Topics in Power Electronics*, vol. 10, no. 2, pp. 1813-1822, 2021.

[12] M. C. Gardner, M. Johnson, and H. A. Toliyat, "Comparison of surface permanent magnet axial and radial flux coaxial magnetic gears," *IEEE Transactions on Energy Conversion*, vol. 33, no. 4, pp. 2250-2259, 2018.

[13] S. Gerber and R. Wang, "Analysis of the end-effects in magnetic gears and magnetically geared machines," *International Conference on Electrical Machines (ICEM)*, pp. 396-402, 2014.

[14] B. Praslicka, M. Johnson, M. C. Gardner, E. Dangtran, and H. A. Toliyat, "Effects of Axial flux magnetic gear misalignment," *IEEE Energy Conversion Congress and Exposition (ECCE)*, pp. 293-300, 2020.

[15] Y. Chen, W. N. Fu, S. L. Ho, and H. Liu, "A quantitative comparison analysis of radial-flux, transverse-flux, and axial-flux magnetic gears," *IEEE Transactions on Magnetics*, vol. 50, no. 11, pp. 1-4, 2014

[16] M. Abolghasemi, A. Ghaheri, A. Harooni, and S. E. Afjei, "Torque Profile Enhancement of a Coaxial Transverse-Radial Flux Magnetic Gear Using Taguchi Optimization Method," *13th International Symposium on Advanced Topics in Electrical Engineering (ATEE)*, pp. 1-6, 2023.

[17] M. Abolghasemi, A. Ghaheri, S. M. Saghin and S. E. Afjei, "Multi-Objective Optimization of an Axial-Flux Magnetic Gear Using Taguchi Method," *14th Power Electronics, Drive Systems, and Technologies Conference (PEDSTC)*, pp. 1-8, 2023.

[18] C.-C. Hwang, P.-L. Li, F. C. Chuang, C.-T. Liu, and K.-H. Huang, "Optimization for Reduction of torque ripple in an axial flux permanent magnet machine," *IEEE Transactions on Magnetics*, vol. 45, no. 3, pp. 1760-1763, 2009.

[19] G. Ruiz-Ponce, M. A. Arjona, C. Hernandez, and R. Escarela-Perez, "Design optimization of an axial-flux magnetic gear by using reluctance network modeling and genetic algorithm," *Energies*, Art. No. 1852, 2023.

[20] S. Mollaie Saghin, A. Ghaheri, and E. Afjei, "Design and Optimization of a Magnetic Geared Permanent Magnet Machine with Iron Pieces Rotor," *Journal of Electrical Engineering & Technology*, vol. 20, pp. 5283-5296, 2025.

[21] H. T. Wang, Z. J. Liu, S. X. Chen and J. P. Yang, "Application of Taguchi method to robust design of BLDC motor performance," *IEEE Transactions on Magnetics*, vol. 35, no. 5, pp. 3700-3702, Sept. 1999.

[22] K. Diao, X. Sun, G. Lei, G. Bramerdorfer, Y. Guo and J. Zhu, "Robust design optimization of switched reluctance motor drive systems based on system-level sequential Taguchi method," *IEEE Transactions on Energy Conversion*, vol. 36, no. 4, pp. 3199-3207, 2021.

[23] C. Qu, Z. Guo, Y. Hu, X. Wang, F. Han, "Multi-objective optimization design of a new permanent magnet synchronous motor based on the Taguchi Method," *Energies*, Art. No. 7347, 2022.

[24] A. Harooni, M. Abolghasemi, A. Ghaheri, and E. Afjei, "Enhancing an Axial Flux Halbach Array Magnetic Gear Torque Profile Using the Taguchi Method," *International Journal of Numerical Modelling: Electronic Networks, Devices and Fields*, vol. 38, no. 3, Art. No. 70014, 2025.

[25] M. Mardani, M. Abolghasemi, A. Ghaheri and S. E. Afjei, "Optimization and Enhancing the Torque Profile of a Novel Double-Layer Radial-Flux Magnetic Gear Using a DOE Method," *5th International Conference on Electrical Machines and Drives (ICEMD)*, pp. 1-8, 2025.

[26] J. Cui, W. Xiao, W. Zou, S. Liu, and Q. Liu, "Design optimisation of submersible permanent magnet synchronous motor by combined DOE and Taguchi approach," *IET Electric Power Applications*, vol. 14, no. 6, pp. 1060-1066, 2020.

[27] A. S. Cabuk, "Investigation of the Vibration Effects on an Outer Rotor Brushless Direct Current Motor," *IEEE Access*, vol. 13, pp. 128262–128279, 2025.